



Open camera or QR reader and scan code to access this article and other resources online.

ORIGINAL ARTICLE

Origami-Based Flexible Robotic Grippers via Hard-Soft Coupled Multimaterial 3D Printing

Wenbo Xue,¹ Liuchao Jin,^{1,2} Bingcong Jian,^{1,3} and Qi Ge¹

Abstract

This study explores the design and performance of origami robotic grippers fabricated through hard-soft coupled multimaterial three-dimensional (3D) printing. We evaluate the impact of design parameters on the kinematic behavior and mechanical functionality of the gripper. A kinematic model is employed to characterize the reachable workspace and motion capabilities, revealing that variations in geometric parameters significantly influence the origami gripper's performance. Furthermore, we explore the mechanical properties of the gripper by manipulating parameters such as soft hinge thickness and crease design, establishing a comprehensive relationship between geometric design and mechanical response. Experimental evaluations demonstrate the interplay between bending angle, force–displacement characteristics, and stiffness in the origami grippers. This research contributes to the optimization of origami-inspired robotic structures, highlighting the potential of multimaterial 3D printing techniques in developing flexible, adaptive, and efficient robotic applications.

Keywords: origami robotic grippers, multimaterial 3D printing, hard-soft coupling, flexible robotics, design optimization

Introduction

Soft robots refer to robots composed of soft materials.¹ Due to their inherent characteristics such as low modulus, high flexibility, as well as the excellent capability of adapting to complex environments and building safe interaction with humans, soft robots have found various applications, including locomotion,^{2–5} manipulation,^{6–9} biomedical devices,^{10–12} and others.^{13–19} However, compared to rigid robots, soft robots still have significant limitations in terms of load capacity and positioning accuracy. The intrinsic low stiffness of the soft materials makes the soft robotic system incompetent in tasks requiring high load capacity, such as

grasping and manipulation of heavy objects.^{20,21} Large deformation on soft robots that have infinite degrees of freedom leads to nonlinear characteristics, which makes precise control and modeling of their position and motion extremely challenging.^{22–25}

It is worth noting that many animals, such as mammals, birds, and fishes, have rigid skeletons for precise and powerful motion, and soft muscles and tissues for compliant interactions with the environment. Inspired by nature, researchers have proposed rigid–flexible coupled robotic systems to expand their capabilities.^{26–32} In these attempts, the rigid skeletons not only enhance the stiffness in specific directions but also reduce the passive deformation in undesired directions.

¹Shenzhen Key Laboratory for Additive Manufacturing of High-Performance Materials, Department of Mechanical and Energy Engineering, Southern University of Science and Technology, Shenzhen, China.

²Department of Mechanical and Automation Engineering, The Chinese University of Hong Kong, Hong Kong, China.

³School of Mechanical Engineering, Tongji University, Shanghai, China.

However, in most of these cases, the rigid components are arranged in the same plane, so that the developed actuators only exhibit single-mode and unidirectional bending. In addition, it is still challenging to achieve precise motion control due to the nonlinearities of the soft materials, especially in the presence of a payload.²⁴

Origami is the traditional art of folding papers into three-dimensional (3D) models. Due to their high flexibility, large contraction ratio, and low costs, origami structures have been widely used in various engineering applications including aerospace,^{33–35} architectures,^{36–38} medical devices,^{11,39–41} as well as robots.^{42–47} In these engineering applications, an origami structure can usually be idealized as rigid panels connected with hinges which the rigid panels can rotate about. Therefore, compared with soft robots which are made of pure soft materials, the panel-hinge system endows origami robots with not only adequate flexibility but also much higher load capacity. More importantly, an origami robot has limited degrees of freedom, and its motion can be precisely modeled and controlled. Due to the above advantages, origami structures have been widely used to form various robots such as walking robots,^{45,48} variable wheel robots,^{42,49} robotic arms,^{50,51} and crawling robots.^{52,53} Despite the rapid advances in applications of origami robots, the main methods to fabricate them rely on the procedures of cutting papers or polymer sheets,^{36,45,54} and manually assembling multiple layers of sheets made of different materials.^{36,54–56} These methods are inefficient and constrain the design flexibility and performance of the fabricated origami robots.

3D printing is an emerging advanced manufacturing technology that allows us to fabricate intricate 3D objects in freeform shapes and is considered as an ideal approach to manufacturing origami robots. Among all the 3D printing technologies, fused deposition modeling (FDM) prints structures with engineering polymers such as polylactic acid (PLA), thermoplastic polyurethane (TPU), polyethylene glycol terephthalate (PET), and many others, which ensure high mechanical robustness of the printed structure. Therefore, FDM has been widely used to print origami robots.^{57,58} Moreover, the multimaterial FDM 3D printing capability is desired to fabricate origami robots with rigid panels rotating about flexible hinges. Arrieta et al. introduced a bioinspired spring origami gripper where the rigid facets with PLA were directly printed on the soft substrate with TPU.^{55,56} However, to avoid the delamination between the dissimilar materials, bolts were used to fix the two materials. Ye et al. reported a wrapping method to address the delamination issue in printing hard-soft coupled origami structures.⁵⁹ However, this method requires the soft material to cover the whole structure regardless of the thickness of the soft hinges, which leads to unnecessary extension of the 3D printing time. Moreover, multimaterial FDM 3D printing has not yet been extensively applied to fabricate the hard-soft coupled origami robotic structure due to the lack of efficient design tools which build the relation between design parameters and motions of the origami robots.

In this article, we introduce a powerful multimaterial FDM 3D printing method with strong interface bonding between hard and soft materials, enabling us to manufacture origami grippers with both foldable characteristics and strong mechanical performance. Compared to previous studies,^{59–61}

this method further enhances the efficiency of 3D printing manufacturing. The design method proposed in this paper for the interface bonding of hard and soft materials can appropriately match the relationship between interface bonding strength and printing time. Specifically, rigid PLA and flexible TPU components are mutually penetrated between printing layers, ensuring that they will not separate even under large deformations, and reducing the manufacturing time with the same printing area. The proposed multimaterial 3D printing method is versatile and user-friendly for users without a chemical background. Using this method, we successfully printed foldable origami grippers consisting of three fingers based on the Yoshimura folding pattern. These origami grippers were manufactured using a commercial FDM printer equipped with two nozzles, capable of simultaneously printing TPU and PLA in a single printing process. By optimizing the design and printing parameters, the printed origami test units could be compressed by 50% under a load of 150 N. Origami tubes can bend over 90° by controlling cable-driven and complete a bending-recovery cycle in as fast as 0.625 s. After studying the bending angle characteristics, stiffness characteristics, and reachable workspace of origami tubes, a flexible robotic gripper was assembled from three origami tubes and a servo motor. The gripper could open and close by driving the cable displacement synchronously, thereby releasing and grabbing fragile objects. The proposed method opens a new and efficient pathway for manufacturing origami robots with broader efficiency and performance.

Results and Discussion

Multimaterial 3D printing of hard-soft coupled origami structures

As illustrated in Figure 1a, we use a commercial FDM multimaterial 3D printer (Ultimaker S5, The Netherlands) to print a Yoshimura origami 2D pattern with length l and height h . Figure 1b presents the repeating unit design for the Yoshimura origami pattern consisting of hard panels (PLA) and soft hinges (TPU). To ensure a strong interfacial bonding between the hard panel and soft hinge, as depicted in Figure 1c, we propose a mutual penetrating approach to design the hard-soft interface where d is the interfacial depth; t_0 is layer thickness (t_0 is 0.1 mm determined by the printer); t_h and t_s are the thicknesses of the hard panel and soft hinge respectively. Figure 1d demonstrates the process of fabricating a 3D origami tube by folding the printed Yoshimura origami sheet and adhering the two edges. Due to the high flexibility, the origami tube exhibits large angle bending when a moment is exerted.

Since the origami sheet is 3D printed with two dissimilar materials (PLA for hard panels and TPU for soft hinges), the interfacial bond between them is weak if the interface is not specially designed (direct neighboring interface in Fig. 1e). To improve the interfacial bonding, we propose the mutual penetrating interface design (mutual penetrating interface in Fig. 1e), where the detailed design parameters are described in Figure 1c. Other than the mutual penetrating approach, the previously reported wrapping approach where the hard panels are wrapped and connected by highly stretchable soft parts (wrapping in Fig. 1e) enables strong interfacial bonding

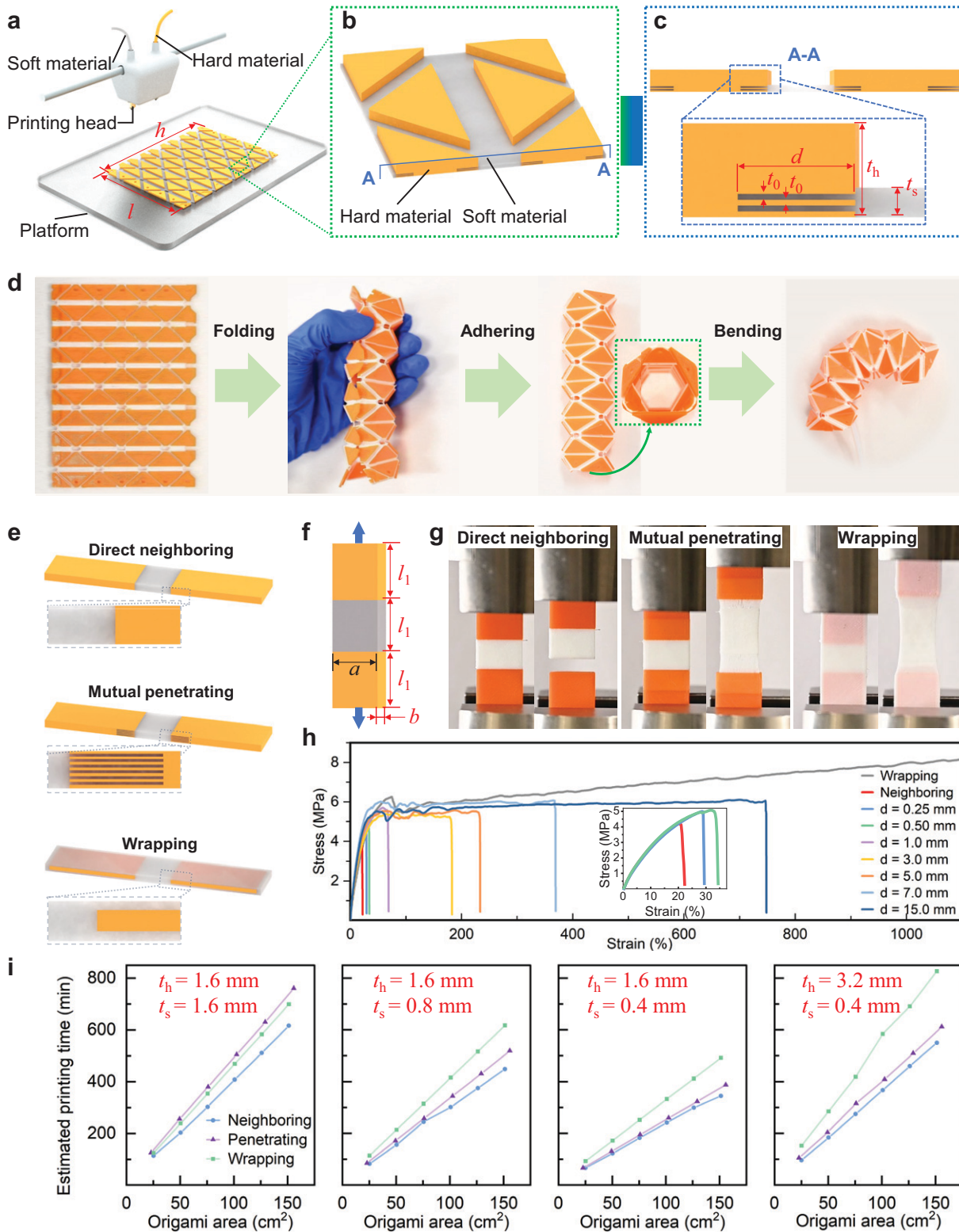


FIG. 1. Multimaterial 3D Printing approaches for fabricating hard-soft coupled origami patterns. **(a)** Illustration of using an FDM multimaterial 3D printer to fabricate a multimaterial origami pattern. **(b)** Zoomed-in view of a hard-soft coupled origami unit pattern. **(c)** Side-view illustration of the origami unit pattern showing that the hard and soft materials are mutually penetrated. **(d)** Snapshots of the process that transforms a flat crease origami pattern into a 3D origami structure. **(e)** Illustrations of three different designs for forming the hard-soft interface in origami structures. **(f-h)** Uniaxial tensile tests to compare the mechanical performance of the hard-soft-hard samples printed using three different interface designs: detailed sample dimensions in **(f)**, snapshots of samples stretched by over 50% in **(g)**, and stress-strain curves in **(h)**. **(i)** Comparison of the estimated time for printing origami patterns using three different interface designs. 3D, three-dimensional; FDM, fused deposition modeling.

between hard and soft parts and has been successfully used to fabricate thick-panel origami structures.⁵⁹ In Figure 1f, we design a uniform hard-soft-hard (HSH) specimen for uniaxial tensile tests to quantitatively investigate the stress-strain relationship of the samples with the three different interfacial designs. As demonstrated in Figure 1g, the tensile stress easily separates hard and soft parts of the specimen with the direct neighboring interfacial design; in contrast, the HSH specimens with the mutual penetrating and wrapping interfacial designs can sustain more than 100% strain without apparent delamination at the interface. Figure 1h presents uniaxial tensile tests on the HSH specimens with the three interfacial designs. For the specimen with the direct neighboring interface, the hard and soft parts delaminate when the applied stress is only 4.03 MPa and the specimen deforms by 22.3%. For the specimens with mutual penetrating interface, the failure strain increases from 28.9% to 746.8% by raising the interfacial depth d from 0.25 to 15 mm. In the origami application, the deformation of the soft hinge is usually less than 50.0%. Therefore, in this work, d is set to be 2.0 mm for fabricating the robotic finger. The specimen with wrapping interface design exhibits the strongest interfacial bonding, and it is not yet damaged even under a large deformation of over 1100%.

When constructing origami structures through multimaterial 3D printing, the printing time is also an important consideration. In Figure 1i, we compare the estimated printing time for printing the same origami patterns (in Fig. 1a) with different interfacial designs. We use the 3D printing slicing software (Ultimaker Cura 5.5.0, Ultimaker, Netherlands) to evaluate the printing time for those origami patterns. The basic parameters for estimation include layer thickness (0.1 mm), line width (0.4 mm), printing speed for PLA (40 mm/s), and printing speed for TPU (20 mm/s). As shown in Figure 1i, in general, the increase in origami area requires more printing time. In the case when the hard panel and soft hinge have the same thickness ($t_h = 1.6$ mm, and $t_s = 1.6$ mm), printing an origami pattern with the direct neighboring interface requires the least time; the time to print the origami pattern with the mutual penetrating interface is slightly higher than that to print the one with wrapping interface. However, when the soft layer hinge thickness (t_s) is lower than the hard panel thickness (t_h), the time to print the origami pattern with the wrapping interface becomes highest. This is because for the origami pattern with direct neighboring or mutual penetrating interface, once the printing of the soft hinge is complete, the remaining parts only need single material (hard material) printing mode to finish; in contrast, for the origami pattern with wrapping interface, the multimaterial (hard and soft materials) printing mode covers the entire process which requires more time as the printing speed for TPU is only half of that for PLA and the two-material-switching steps take additional time. After comparing Figure 1h and i, we conclude that the mutual penetrating interfacial design offers reasonably good interfacial bonding between the hard panel and soft hinge, and requires less time to print an origami pattern with the thick hard panel and the thin soft hinge compared with the wrapping interfacial design. Therefore, in this work, we use the mutual penetrating interfacial design for the following origami-based robotic structures.

Design for hard-soft coupled origami-based robotic finger

As illustrated in Figure 2a, we fabricate an origami gripper by assembling three origami fingers onto a 3D-printed base. The origami fingers are actuated by cable driving. One end of the driving cable is attached to the tip of the origami finger, and the other end of the cable is mounted to the pulley of a servo motor fixed on the back of the 3D-printed base. When the servo motor turns on, the rotation of the pulley pushes the driving cables, resulting in the bending of the three origami fingers (Fig. 2b), which is closely related to the geometric parameters of the origami structures. Therefore, it is necessary to develop a model that connects the bending kinematics and geometric parameters of the origami finger.

Kinematic model of the Yoshimura origami structure

Figure 3a–c illustrates the ideal zero-thickness model of the Yoshimura origami unit cell that is used to form the origami finger. The Yoshimura origami unit cell can be described by three equilateral triangle planes: $\Delta A_1A_2A_3$, $\Delta B_1B_2B_3$, and $\Delta C_1C_2C_3$. The length of each equilateral triangle is L , and the height of each isosceles triangle panel is h . The height of the unit cell is H_0 . The deformation of the origami unit cell can be described by the coordinate system $o_0\text{-}\mathbf{x}_0\text{-}\mathbf{y}_0\text{-}\mathbf{z}_0$, which is fixed at the center of the bottom triangle plane $\Delta A_1A_2A_3$. In the center of the top triangle $\Delta B_1B_2B_3$, we set a coordinate system $o_1\text{-}\mathbf{x}_1\text{-}\mathbf{y}_1\text{-}\mathbf{z}_1$. To facilitate the geometric analysis, we set the middle points for lines A_1A_3 , B_1B_3 , and C_2C_3 as point M_1 , point M_2 , and point M_3 , respectively.

Before bending deformation, the coordinates of the three vertices of $\Delta A_1A_2A_3$ and $\Delta B_1B_2B_3$ are \mathbf{p}_{A_i} and \mathbf{p}_{B_i} in the $o_0\text{-}\mathbf{x}_0\text{-}\mathbf{y}_0\text{-}\mathbf{z}_0$ system are as follows:

$$\begin{aligned} \mathbf{p}_{A_1} &= \left[\frac{L}{2} \quad \frac{\sqrt{3} \cdot L}{6} \quad 0 \right]^T, & \mathbf{p}_{A_2} &= \left[0 \quad -\frac{\sqrt{3} \cdot L}{3} \quad 0 \right]^T, \\ \mathbf{p}_{A_3} &= \left[-\frac{L}{2} \quad \frac{\sqrt{3} \cdot L}{6} \quad 0 \right]^T, & & (1) \\ \mathbf{p}_{B_1} &= \left[\frac{L}{2} \quad \frac{\sqrt{3} \cdot L}{6} \quad H_0 \right]^T, & \mathbf{p}_{B_2} &= \left[0 \quad -\frac{\sqrt{3} \cdot L}{3} \quad H_0 \right]^T, \\ \mathbf{p}_{B_3} &= \left[-\frac{L}{2} \quad \frac{\sqrt{3} \cdot L}{6} \quad H_0 \right]^T, & & (2) \end{aligned}$$

Here, H_0 is the height of the origami unit cell which can be expressed by h and L :

$$H_0 = 2\sqrt{h^2 - \left(\frac{\sqrt{3}}{6} \cdot L\right)^2}. \quad (3)$$

Figure 3d illustrates the bending motion of the origami unit cell by using the sectional views, which are cut by the $\mathbf{y}_0\text{-}\mathbf{z}_0$ plane where the points A_2 , B_2 , C_1 , M_1 , M_2 , and M_3 are located. During bending deformation, the bottom triangle $\Delta A_1A_2A_3$ is stationary, but the middle and top triangular planes are tilted. In the counterclockwise bending, the

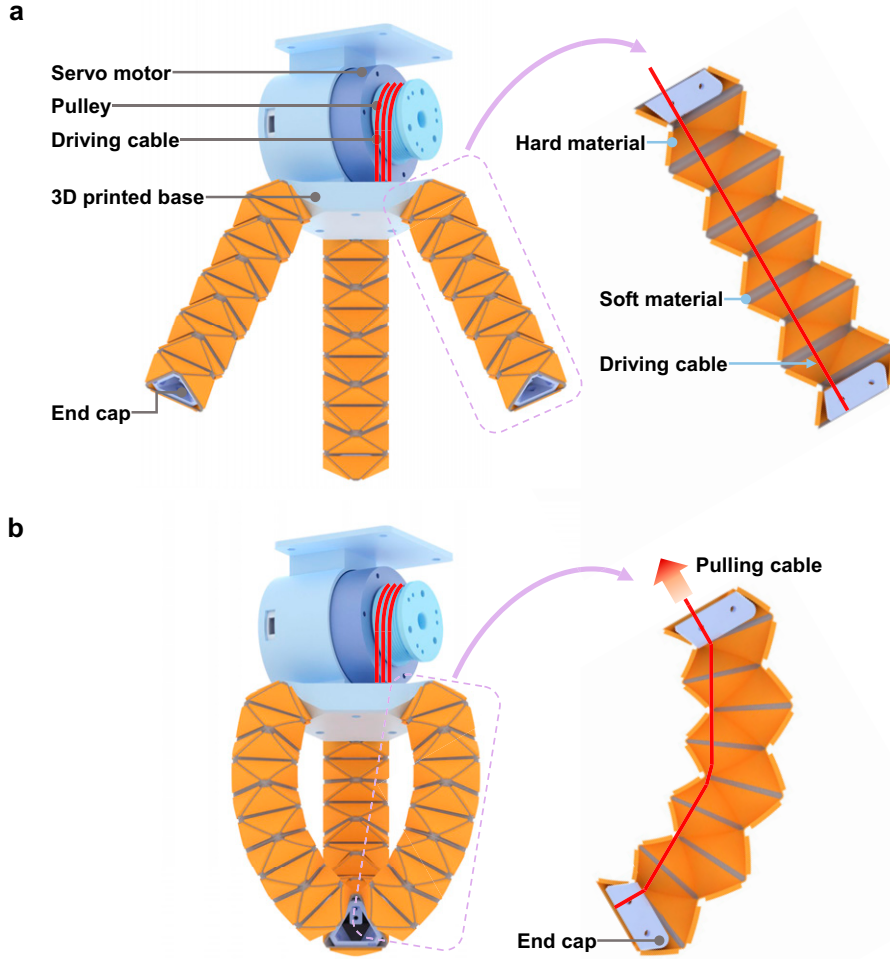


FIG. 2. Schematic illustration of the origami fingers. **(a)** Relaxed state of the origami fingers. **(b)** Grasping state of the origami fingers.

origami unit cell reaches the maximum bending angle when vertex B_2 arrives at the bottom triangle plane $\Delta A_1 A_2 A_3$; in the clockwise bending, the origami finger reaches the maximum bending angle when middle C_1 arrives at the bottom triangle plane $\Delta A_1 A_2 A_3$. In Figure 3e, we use the counterclockwise bending scenario to conduct the geometric analysis, which helps us calculate the coordinates $\tilde{\mathbf{p}}_{B_i}$ of the three vertices $\Delta B_1 B_2 B_3$ after bending. As shown in Figure 3e, during bending, the lines $\overline{A_2 M_1}$, $\overline{B_2 M_2}$, and $\overline{C_1 M_3}$ converge to a point G . The angle between the $\overline{A_2 M_1}$ and $\overline{B_2 M_2}$ is α , so that $\angle A_2 G B_2 = \alpha$. $\angle A_2 G B_2$ is equally divided by line $\overline{C_1 G}$ into two angles ($\angle A_2 G C_1 = \angle C_1 G B_2 = \beta = \alpha/2$). During counterclockwise bending, α varies from 0° to α_{\max}^+ :

$$\cos \frac{\alpha_{\max}^+}{2} = \frac{(l_{A_2 M_3} + l_{M_3 C_1})^2 + (l_{A_2 M_1})^2 - (l_{M_1 C_1})^2}{2 \cdot (l_{A_2 M_3} + l_{M_3 C_1}) \cdot (l_{A_2 M_1})}. \quad (4)$$

where $l_{A_2 M_3}$, $l_{M_3 C_1}$, $l_{A_2 M_1}$, and $l_{M_1 C_1}$ are the lengths of the lines between the corresponding vertex.

The variation of α leads to the changes of other angles such as β , γ , θ_1 , and θ_2 . θ_1 and θ_2 can be calculated based on the relation between vectors $\mathbf{l}_{A_2 M_3}$, $\mathbf{l}_{M_3 C_1}$, $\mathbf{l}_{A_2 M_1}$, and $\mathbf{l}_{M_1 C_1}$:

$$\mathbf{l}_{A_2 M_3} + \mathbf{l}_{M_3 C_1} = \mathbf{l}_{A_2 M_1} + \mathbf{l}_{M_1 C_1}. \quad (5)$$

Eq. 5 can be extended in component form:

$$\begin{aligned} l_{A_2 M_3} \cdot \cos \theta_1 + l_{M_3 C_1} \cdot \cos(\alpha/2) - l_{M_1 C_1} \cdot \cos \theta_2 - l_{A_2 M_1} \cdot \cos 0 &= 0, \\ l_{A_2 M_3} \cdot \sin \theta_1 + l_{M_3 C_1} \cdot \sin(\alpha/2) - l_{M_1 C_1} \cdot \sin \theta_2 - l_{A_2 M_1} \cdot \sin 0 &= 0, \end{aligned} \quad (6)$$

so that θ_1 and θ_2 can be expressed by the variable α and other geometric parameters. Detailed solving processes for Eq. 6 can be found in Supplementary Materials.

Once θ_1 is calculated, one can have the expression for the vector $\mathbf{l}_{A_2 M_3}$:

$$\mathbf{l}_{A_2 M_3} = [0 \quad l_{A_2 M_3} \cdot \cos \theta_1 \quad l_{A_2 M_3} \cdot \sin \theta_1]^T. \quad (7)$$

$\mathbf{l}_{A_2 M_3}$ can also be calculated by the current positions of vertices A_2 and M_3 :

$$\mathbf{l}_{A_2 M_3} = \tilde{\mathbf{p}}_{M_3} - \tilde{\mathbf{p}}_{A_2} = [0 \quad \tilde{y}_{M_3} - \tilde{y}_{A_2} \quad \tilde{z}_{M_3} - \tilde{z}_{A_2}]^T. \quad (8)$$

A_2 is stationary, so that $\tilde{\mathbf{p}}_{A_2} = \mathbf{p}_{A_2}$ ($\tilde{y}_{A_2} = -\sqrt{3} \cdot L/3$, $\tilde{z}_{A_2} = 0$). By comparing Eqs. 7 and 8, we can have the current position of vertex of M_3 :

$$\tilde{\mathbf{p}}_{M_3} = \begin{bmatrix} 0 & \underbrace{-\frac{\sqrt{3}L}{3} + l_{A_2 M_3} \cdot \cos \theta_1}_{\tilde{y}_{M_3}} & \underbrace{l_{A_2 M_3} \cdot \sin \theta_1}_{\tilde{z}_{M_3}} \end{bmatrix}^T. \quad (9)$$

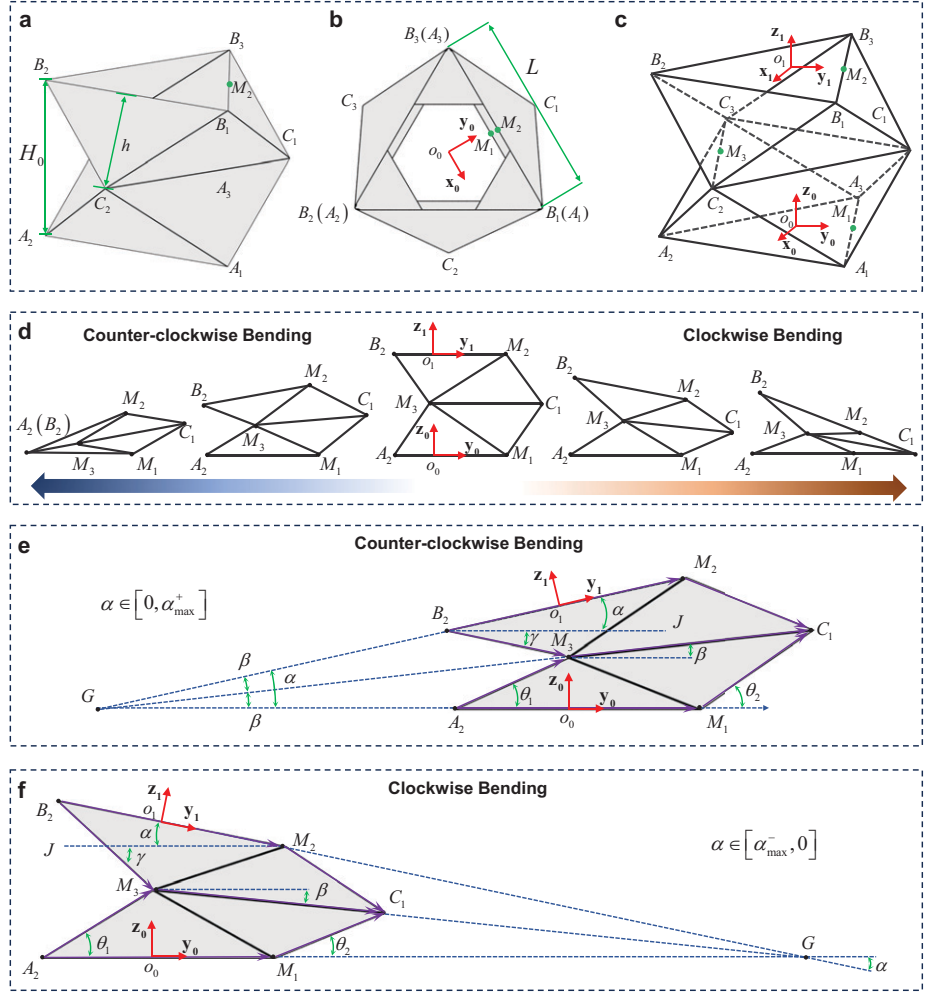


FIG. 3. Origami unit movement analysis. (a) Top and bottom isometric views of the origami unit. (b) Top view of the origami unit. (c) Wireframe diagram of the origami unit. (d) Schematic representation of the forward and backward bending process of the origami unit in wireframe diagram. (e) Geometric illustration of the counterclockwise bending motion of the origami unit. (f) Geometric illustration of the clockwise bending motion of the origami unit.

Similarly, we can have the expression for the vector $\mathbf{l}_{B_2M_3}$ as follows:

$$\mathbf{l}_{B_2M_3} = [0 \quad l_{B_2M_3} \cdot \cos \gamma \quad -l_{B_2M_3} \cdot \sin \gamma]^T. \quad (10)$$

where γ is a function of α ($\gamma = \theta_1 - \alpha$). $\mathbf{l}_{B_2M_3}$ can also be calculated by the current positions of vertices B_2 and M_3 :

$$\mathbf{l}_{B_2M_3} = \tilde{\mathbf{p}}_{M_3} - \tilde{\mathbf{p}}_{B_2} = [0 \quad \tilde{y}_{M_3} - \tilde{y}_{B_2} \quad \tilde{z}_{M_3} - \tilde{z}_{B_2}]^T. \quad (11)$$

Since $\tilde{\mathbf{p}}_{M_3}$ has already been calculated in Eq. 9, by comparing Eqs. 10 and 11, we can have the current position of vertex of B_2 :

$$\tilde{\mathbf{p}}_{B_2} = \begin{bmatrix} 0 \\ \underbrace{-\frac{\sqrt{3} \cdot L}{3} + l_{A_2M_3} \cdot \cos \theta_1 - l_{B_2M_3} \cdot \cos(\theta_1 - \alpha)}_{\tilde{y}_{B_2}} \\ \underbrace{l_{A_2M_3} \cdot \sin \theta_1 + l_{B_2M_3} \cdot \sin(\theta_1 - \alpha)}_{\tilde{z}_{B_2}} \end{bmatrix}^T. \quad (12)$$

Similarly, we can have the expression for the vector $\mathbf{l}_{B_2M_2}$ as follows:

$$\mathbf{l}_{B_2M_2} = [0 \quad l_{B_2M_2} \cdot \cos \alpha \quad l_{B_2M_2} \cdot \sin \alpha]^T. \quad (13)$$

$\mathbf{l}_{B_2M_2}$ can also be calculated by the current positions of vertices B_2 and M_2 :

$$\mathbf{l}_{B_2M_2} = \tilde{\mathbf{p}}_{M_2} - \tilde{\mathbf{p}}_{B_2} = [0 \quad \tilde{y}_{M_2} - \tilde{y}_{B_2} \quad \tilde{z}_{M_2} - \tilde{z}_{B_2}]^T. \quad (14)$$

Since $\tilde{\mathbf{p}}_{B_2}$ vector is known in Eq. 12, by comparing Eqs. 13 and 14, we can have the current position of vertex of M_2 :

$$\tilde{\mathbf{p}}_{M_2} = \begin{bmatrix} 0 \\ \underbrace{\tilde{y}_{B_2} + l_{B_2M_2} \cdot \cos \alpha}_{\tilde{y}_{M_2}} \\ \underbrace{\tilde{z}_{B_2} + l_{B_2M_2} \cdot \sin \alpha}_{\tilde{z}_{M_2}} \end{bmatrix}^T. \quad (15)$$

By comparing Figure 3c with e, and since point M_2 is the center of symmetry for vertices B_1 and B_3 , we can easily calculate its coordinates during the bending process:

$$\tilde{\mathbf{p}}_{B_1} = \left[\frac{L}{2} \quad \tilde{y}_{M_2} \quad \tilde{z}_{M_2} \right]^T, \quad \tilde{\mathbf{p}}_{B_3} = \left[-\frac{L}{2} \quad \tilde{y}_{M_2} \quad \tilde{z}_{M_2} \right]^T. \quad (16)$$

Using Eqs. 12 and 16, we can calculate the coordinates $\tilde{\mathbf{p}}_{B_i}$ of the vertices in the top triangle during counterclockwise bending. The geometric parameters used to compute $\tilde{\mathbf{p}}_{B_i}$ can be found in Table 1.

Using the same analysis procedure, we can also calculate the coordinates $\tilde{\mathbf{p}}_{B_i}$ of the vertices in the top triangle during clockwise bending (Fig. 3f) during which α varies from 0° to α_{\max}^- ($\alpha_{\max}^- = -\alpha_{\max}^+$).

TABLE 1. GEOMETRIC PARAMETERS OF A YOSHIMURA ORIGAMI UNIT CELL IN FIGURE 3

Geometric parameter	$l_{A_2M_3}$	$l_{M_3C_1}$	$l_{A_2M_1}$	$l_{M_1C_1}$	$l_{B_2M_3}$	$l_{B_2M_2}$	$l_{M_2C_1}$
Value	h	L	L	h	h	L	h

Once we know the coordinates $\tilde{\mathbf{p}}_{B_i}$ of the vertices in the top triangle, the geometric center o_1 of the $\Delta B_1B_2B_3$ can be readily calculated:

$$\tilde{\mathbf{p}}_{o_1} = \frac{1}{3} \sum_{i=1}^3 \tilde{\mathbf{p}}_{B_i}. \quad (17)$$

As shown in Figure 4, an origami finger can be assembled by stacking several origami unit cells. Figure 4a illustrates an isometric view of an origami finger with 5 unit cells. As shown in Figure 4b and c, the coordinate system $o_{i-1}\mathbf{x}_{i-1}\mathbf{y}_{i-1}\mathbf{z}_{i-1}$ is fixed to the center of the bottom triangle of the i^{th} unit cell and is the local coordinate system used to describe the motion of the coordinate system $o_i\mathbf{x}_i\mathbf{y}_i\mathbf{z}_i$ which is fixed to the center of its top triangle. In addition, the globe coordinate system $O\mathbf{X}\mathbf{Y}\mathbf{Z}$ is attached to the center of the bottom triangle of unit 1, which is stationary during bending (Fig. 4c). The current position of the center of the top triangle of the i^{th} unit cell can be described by the local coordinate system $o_{i-1}\mathbf{x}_{i-1}\mathbf{y}_{i-1}\mathbf{z}_{i-1}$ (denoted as \mathbf{p}_{o_i}), and can also be described by the globe coordinate system $O\mathbf{X}\mathbf{Y}\mathbf{Z}$ (denoted as \mathbf{P}_{o_i}).

Figure 4c illustrates a counterclockwise bending of the origami finger where the bending angle for each unit cell is α . Thus, the total bending angle of the origami finger is ω ($\omega = 5\alpha$). The bending motion of the origami finger can be simply reflected by the current position of the origami fingertip \mathbf{P}_{o_5} . To derive \mathbf{P}_{o_5} , we first calculate \mathbf{P}_{o_1} , which is the current position of the center of the top triangle of the 1st unit cell described by the globe coordinate system $O\mathbf{X}\mathbf{Y}\mathbf{Z}$. Since $O\mathbf{X}\mathbf{Y}\mathbf{Z}$ coincides with $o_0\mathbf{x}_0\mathbf{y}_0\mathbf{z}_0$, we have

$$\mathbf{P}_{o_1} = \mathbf{p}_{o_1}. \quad (18)$$

For the center of the top triangle of the second unit cell, its current position is \mathbf{P}_{o_2} in the local coordinate system $o_1\mathbf{x}_1\mathbf{y}_1\mathbf{z}_1$ which is rotated by $\mathbf{R}(\alpha)$ with respect to the coordinate system \mathbf{P}_{o_1} . Therefore, its current position \mathbf{P}_{o_2} in the globe coordinate can be calculated as follows:

$$\mathbf{P}_{o_2} = \mathbf{R}(\alpha) \cdot \mathbf{p}_{o_2} + \mathbf{P}_{o_1}. \quad (19)$$

The rotation matrix $\mathbf{R}(\alpha)$ is as follows:

$$\mathbf{R}(\alpha) = \begin{bmatrix} 1 & 0 & 0 \\ 0 & \cos(\alpha) & -\sin(\alpha) \\ 0 & \sin(\alpha) & \cos(\alpha) \end{bmatrix} \quad (20)$$

Following the above analysis, we can express the current position of the i^{th} unit cell in the globe coordinate:

$$\begin{aligned} \mathbf{P}_{o_i} &= \mathbf{R}((i-1) \cdot \alpha) \cdot \mathbf{p}_{o_i} + \mathbf{P}_{o_{i-1}} \\ &= \mathbf{R}(\alpha)^{i-1} \cdot \mathbf{p}_{o_i} + \mathbf{P}_{o_{i-1}} \quad i > 1 \end{aligned} \quad (21)$$

Specifically, the bending deformations of each individual unit cell in Figure 4 are the same. Thus, we have

$$\mathbf{p}_{o_i} = \mathbf{p}. \quad (22)$$

Since the degree of deformation of each origami unit is consistent, the bending angle of each origami unit is α ,

$$\mathbf{P}_{o_5} = \sum_{j=0}^4 \mathbf{R}(\alpha)^j \cdot \mathbf{p}. \quad (23)$$

For an origami finger composed of 5 origami units, the bending angle is as follows:

$$\omega = 5\alpha \quad (24)$$

Due to the rotational symmetry of the origami units, their 3D reachable space is as follows:

$$\mathbf{P}_{O_{5,k}} = \mathbf{R}_z(120^\circ \cdot k) \cdot \mathbf{P}_{o_5} \quad k=0,1,2 \quad (25)$$

where the expression of the rotation matrix rotating 120° multiples around the z -axis is as follows

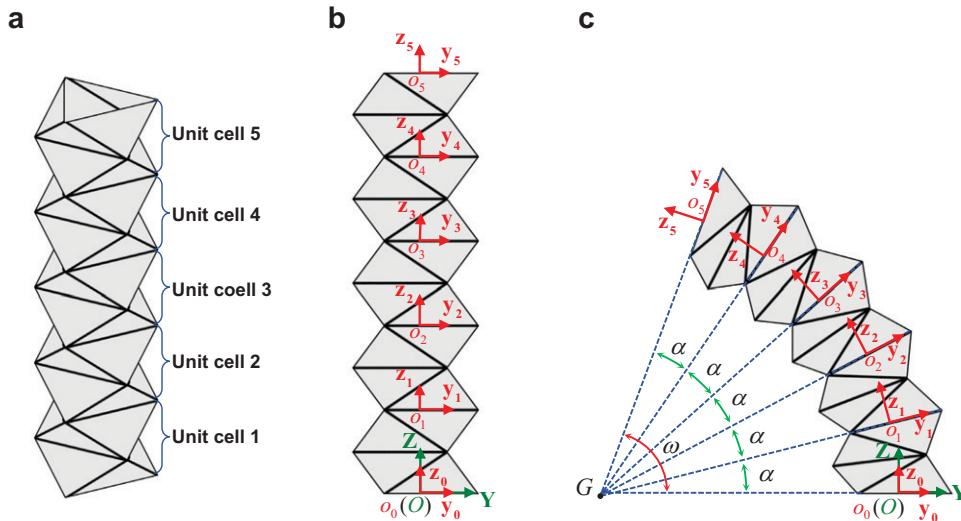


FIG. 4. Origami finger assembly diagram. (a) Side view of the origami finger. (b) Initial undriven state. (c) Bent state.

$$\mathbf{R}_z(120^\circ \cdot k) = \begin{bmatrix} \cos(120^\circ \cdot k) & -\sin(120^\circ \cdot k) & 0 \\ \sin(120^\circ \cdot k) & \cos(120^\circ \cdot k) & 0 \\ 0 & 0 & 1 \end{bmatrix}. \quad (26)$$

The detail of the derivation for motion equations of multiple interconnected origami units is illustrated in Section S2 of Supplementary Materials.

The influence of geometric parameter on Yoshimura origami's behavior

By analyzing the kinematic model of the Yoshimura origami structure, we found that various design parameters affect the reachable workspace. Therefore, we can use the theoretical model to guide structural optimization. Figure 5 illustrates the influence of origami unit parameters (L, h) on the motion capability of the origami structure. Each origami finger in our design consists of several identical origami cells, with five cells chosen for the configuration in this study. These cells are simultaneously manufactured using a multimaterial 3D printer, ensuring geometric consistency across all cells. This uniformity is critical to maintaining the structural integrity and performance consistency of the origami finger during bending motions. To further enhance uniform force distribution, we addressed potential point contact issues between the driving rope and the origami structure at the ends of the finger by incorporating hard end caps. These caps ensure uniform force conditions across all origami cells, preventing localized force transmission and ensuring consistent force distribution during bending. Therefore, during the bending process, each

unit maintains a consistent degree of bending. The center of the origami fingertip, which corresponds to the origin of the coordinate system $O_5\text{-}X_5\text{-}Y_5\text{-}Z_5$, represents the reachable workspace of this section of the origami finger.

When $L = 30$ mm and $h = 15$ mm, the 3D reachable space of the origami unit is depicted in Figure 5a. Figure 5b shows the projection of the motion trace of the center point at the fingertip ($L = 32$ mm, $h = 15$ mm) on the horizontal plane. The trace generally forms radial segments centered around the origin, with adjacent segments separated by angles of approximately 60° . Through the viewport, we can observe the complete motion trace of the center point at the fingertip of the origami finger on the vertical plane. Additionally, as shown in Figure 5c, the origami finger does not exhibit perfect symmetry during clockwise (CW) and counterclockwise (CCW) bending, confirming the asymmetry observed in Figure 3.

With $h = 15$ mm held constantly, we examined the influence of varying L from 20 mm to 44 mm on the motion trace of the fingertip center point on the plane, as depicted in Figure 5d. Similarly, with $L = 32$ mm fixed, we explored how varying h from 10 to 20 mm affected the fingertip's motion trace, as shown in Figure 5e. Based on these kinematic analyses, a model of an origami finger with five units was established for various parameter sets (L, h). Figure 5f presents the maximum displacement of the fingertip center point from the initial central axis (z -axis) as a pseudo-color cloud map. The results indicate that, generally, a decrease in L combined with an increase in h results in a greater displacement from the central axis. We selected the optimal origami unit parameters

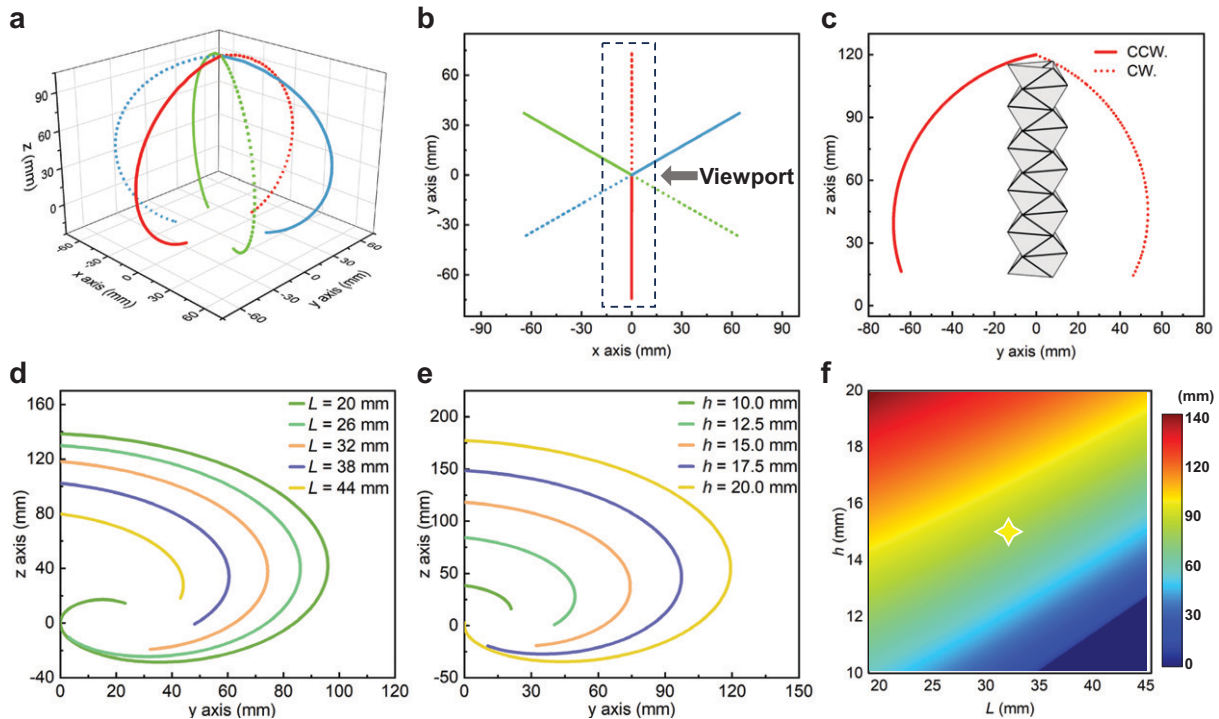


FIG. 5. Analysis of origami unit design parameters. (a) Reachable space of 5 origami units. (b) The projection trace of the spatial motion of the center point at the fingertip of the origami finger on the horizontal plane. (c) The motion trace of the center point at the fingertip of the origami finger on the vertical plane. (d) Motion traces of the origami finger with different design parameters L . (e) Motion traces of the origami finger with different design parameters h . (f) Maximum displacement of the center point at the fingertip relative to the z -axis for different values of h and L .

as $L = 32$ mm and $h = 15$ mm. This configuration, highlighted by a yellow four-pointed star, demonstrates a displacement from the initial central axis of 74.4 mm. The selection of these parameters is not aimed at maximizing the vertical axial offset distance. Instead, they represent a balance between performance, structural stability, and practical manufacturing constraints. Smaller L and larger h values yield a thinner and longer overall finger design, which can increase the fingertip's maximum displacement. However, under the rope-driven actuation condition, the origami finger operates in a compressive stress state. According to material mechanics principles, a slender structure is prone to instability under such stress conditions. Additionally, the selected parameters are influenced by the size of objects we aim to manipulate, such as water bottles, dragon fruits, and apples, which have characteristic diameters of approximately 60 mm. The parameters $L = 32$ mm and $h = 15$ mm are suitable for handling these objects, providing an optimal balance between design functionality and structural integrity. From a manufacturing and assembly perspective, L values smaller than 32 mm pose significant challenges. The assembly process requires manually gluing and fixing the joints of the origami fingers while maintaining pressure on

both sides. A smaller L results in insufficient internal space, making these tasks impractical. Similarly, practical constraints on the maximum achievable h arise from multimaterial printing resolution limitations and structural integrity requirements. Taking these considerations into account, the chosen configuration ($L = 32$ mm, $h = 15$ mm) demonstrates a displacement from the initial central axis of 74.4 mm and achieves a balance between kinematic performance, structural stability, and practical manufacturability.

The design parameters of origami patterns play a crucial role in determining the mechanical response of the resulting 3D origami structures. Figure 6a displays the crease pattern for the Yoshimura origami, which is subsequently used to create the robotic grippers in this study. In the crease pattern, the solid blue line represents the peak creases that bend the structure outward, whereas the dashed red line represents the valley creases that bend the structure inward. To enhance the load-bearing capacity of the 3D origami structure, we increased the thickness of the hard panels (t_h) to 1.6 mm, as shown in Figure 6b. To prevent rotational interference caused by the increased thickness, we adjusted the crease pattern by defining the widths of the valley and peak lines as

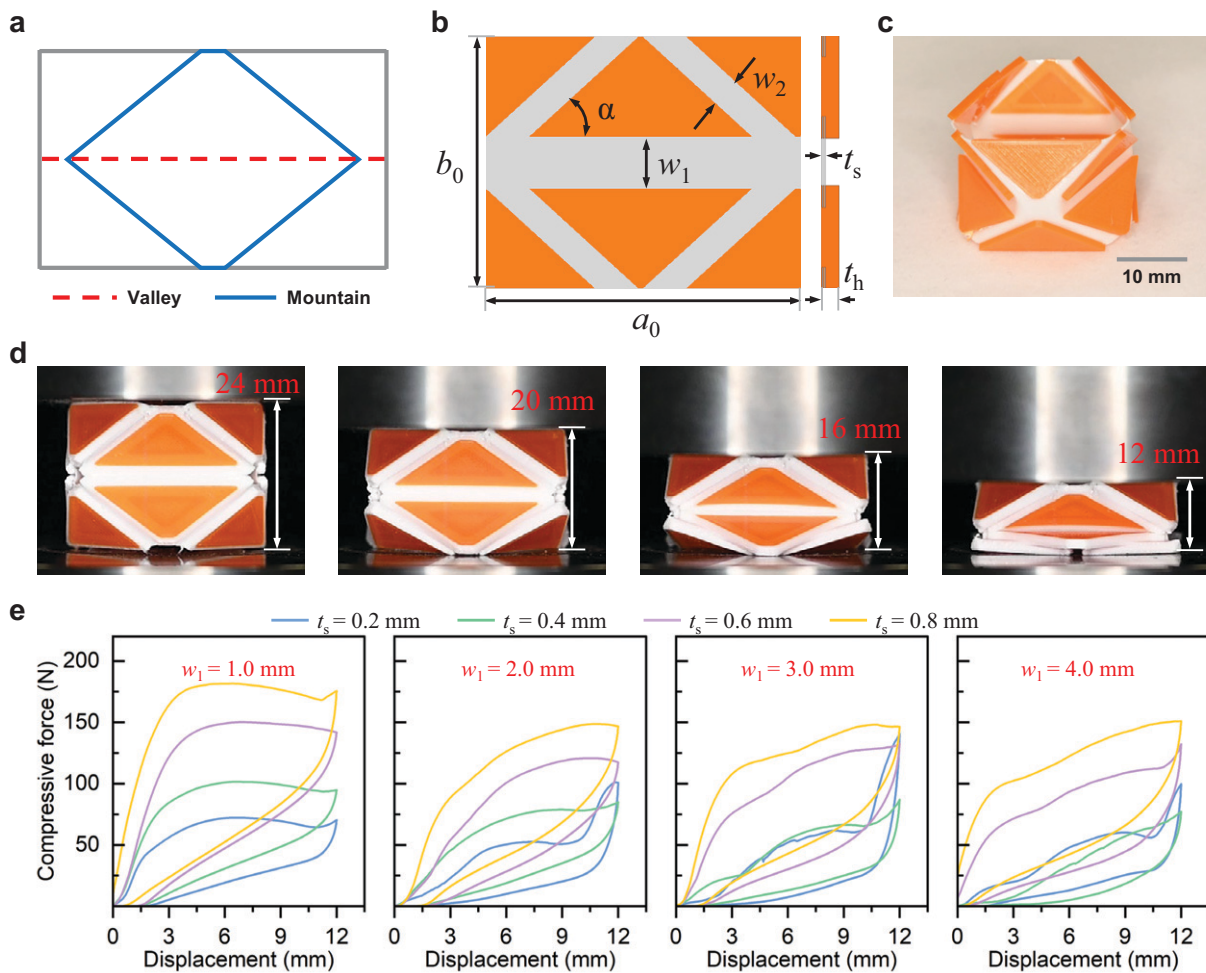


FIG. 6. Relation between origami design and mechanical performance. (a) Representative unit pattern of Yoshimura origami. (b) Key design parameters for a thick panel Yoshimura origami unit pattern. (c) Snapshot of an assembled 3D origami Yoshimura unit. (d) Process of compressing a 3D Yoshimura origami unit. (e) Experimental results of compressing the 3D origami units with different design parameters.

w_1 and w_2 , respectively. Figure 6c illustrates a 3D origami unit cell constructed from the modified Yoshimura pattern (parameters are listed in Table 2). Figure 6d shows the experimental setup where the origami is compressed by 50%.

Previous studies have shown that the width of the valley (w_1) and the thickness of the soft panel (t_s) significantly impact the mechanical behavior of the manufactured origami unit cells, compared to other parameters.^{60,61} Figure 6e presents the force–displacement relationship for origami unit cells with various w_1 and t_s values. From Figure 6e, we observe that with a fixed w_1 , increasing t_s substantially enhances the stiffness of the origami structure, as the majority of deformation during compression occurs at the soft hinges.⁶⁰ Additionally, for structures with the same t_s , an increase in w_1 from 1.0 mm to 2.0 mm results in a marked decrease in stiffness. However, further increases in w_1 have minimal impact on the mechanical response. This phenomenon occurs because, when w_1 is considerably smaller than $2t_h - t_s$, the rotation of hard panels causes significant stretching of the soft hinges, thereby increasing stiffness⁶⁰; when w_1 is near or exceeds $2t_h - t_s$, the deformation of the soft hinges is minimal. Based on Figure 6e, we have chosen to adjust the robotic finger stiffness by varying t_s while keeping other parameters constant, as outlined in Table 1.

In this work, we employ 3D origami tubes (Fig. 1d) as fingers to construct a flexible origami gripper. The bending of the origami fingers is achieved through a cable-driven mechanism, which is illustrated in Supplementary Video S1. Therefore, understanding the bending behavior of the origami tube based on design parameters and cable-driving inputs is essential. Figure 7a illustrates our testing system, which investigates the relationship between the origami bending angle and cable displacement/force. In this system, both the horizontal translational stage and the origami fixture are mounted on an optical table. One end of the origami finger is fixed to the fixture, ensuring that the finger is initially deployed horizontally. The other end of the origami finger is connected to a steel cable (Jiangsu Faersheng Acquisitive Liter Group Co., Ltd., China; diameter: 0.8 mm), which is then attached to a force sensor (Bengbu Dayang Sensing System Engineering Co., Ltd., China; range: 0–1000 N, zero balance: 0.1% FS) mounted on the translation stage (FSK40, Chengdu Fuyu Technology Co., Ltd., China; stroke: 200 mm). When the stage moves leftward, it pulls the cable, resulting in the bending of the origami finger, which is recorded by a camera (Z7II, Nikon Corporation, Japan) positioned in front of the finger. We denote the displacement of the driving cable as Δx , and the bending angle θ is defined as the angle between the origami edge and the y -axis. An increase in Δx causes a corresponding increase in

θ . The variation in the bending angle is measured using an online video frame processing software (Kinovea-0.9.5, open-source software).

Figure 7b shows snapshots of the origami finger at bending angles of 0° , 30° , and 90° . In Figure 7c, we present the relationship between cable displacement and bending angle, which demonstrates good linearity. Achieving a 90° bend in the origami finger requires a cable displacement of 35 mm. Our robotic gripper system integrates three origami fingers driven by a single servo motor. Since the maximum output torque of the servo motor (DM-J4310, DM Technology Co., Ltd., China) is $3 \text{ N}\cdot\text{m}$ and the winding wheel radius is 20 mm, the tension applied to each finger is limited to 50 N. Therefore, it is necessary to investigate the relationship between the force and bending angle (or force and cable displacement) for the origami finger with different soft hinge thicknesses, t_s . As shown in Figure 7d, increasing t_s results in higher bending stiffness. Under the maximum tensile force of 50 N, the maximum bending angle decreases from 130.7° to 106.5° , 67.0° , and 40.7° as t_s increases from 0.2 mm to 0.4 mm, 0.6 mm, and 0.8 mm, respectively.

We further investigate the dynamic bending behavior of the origami finger. Figure 7e shows the dynamic input of the horizontal translational stage, with a displacement amplitude of 35 mm, which corresponds to a 90° bend. The period of the loading–unloading cycle is denoted as T , leading to a cable displacement speed (v) of $(2 \times 35 \text{ mm})/T$. In the dynamic bending behavior characterization, we use origami fingers with a soft hinge thickness (t_s) of 0.4 mm, which can bend up to 90° and provide greater bending stiffness compared to fingers with $t_s = 0.2 \text{ mm}$. Figure 7f presents the dynamic bending responses of the origami finger under varying displacement speeds (or periods). At $T = 70 \text{ s}$ ($v = 1 \text{ mm/s}$), the origami finger exhibits quasi-static bending, achieving a precise range between 0° and 90° . As T decreases to 14 s, 4.7 s, and 2.3 s (corresponding to $v = 5 \text{ mm/s}$, 15 mm/s, and 30 mm/s), the bending amplitude slightly decreases but remains around 80° due to the high elasticity of the soft hinges.

In this work, we utilize three origami fingers to form a gripper. Therefore, the bending stiffness of each finger is crucial for the performance of grasping target objects. To investigate this, we set up a testing system, as shown in Figure 8a, to evaluate the bending stiffness of the origami finger at various bending angles. In this system, the origami finger is fixed to a goniometric stage. By adjusting the goniometric stage, we ensure that the top surface of the origami finger, at any given bending angle, is parallel to the optical table surface where the translation and goniometric stages are mounted. During testing, the translational stage moves rightward, causing a contact plate to push against the tip of the origami finger. A force sensor between the contact plate and the translational stage measures the resulting force. Figure 8b displays snapshots of the origami fingers at different bending angles ($\theta = 0^\circ$, 25° , 50° , and 75°). By adjusting the rotational angle of the goniometric stage, we maintain the top surface of the origami finger horizontally aligned, ensuring the force from the contact plate is normal to the tangential direction of the fingertip.

Figure 8c shows the force–displacement curves recorded for the origami fingers with various soft hinge thicknesses ($t_s = 0.2 \text{ mm}$, 0.4 mm, 0.6 mm, and 0.8 mm) and bending

TABLE 2. GEOMETRIC PARAMETERS USED TO MANUFACTURE THREE-DIMENSIONAL ORIGAMI STRUCTURE

Geometric parameter	Value	Unit
t_s	0.4	mm
t_h	1.6	mm
w_1	2.0	mm
w_2	1.0	mm
α	42.5	$^\circ$
a_0	32	mm
b_0	25	mm

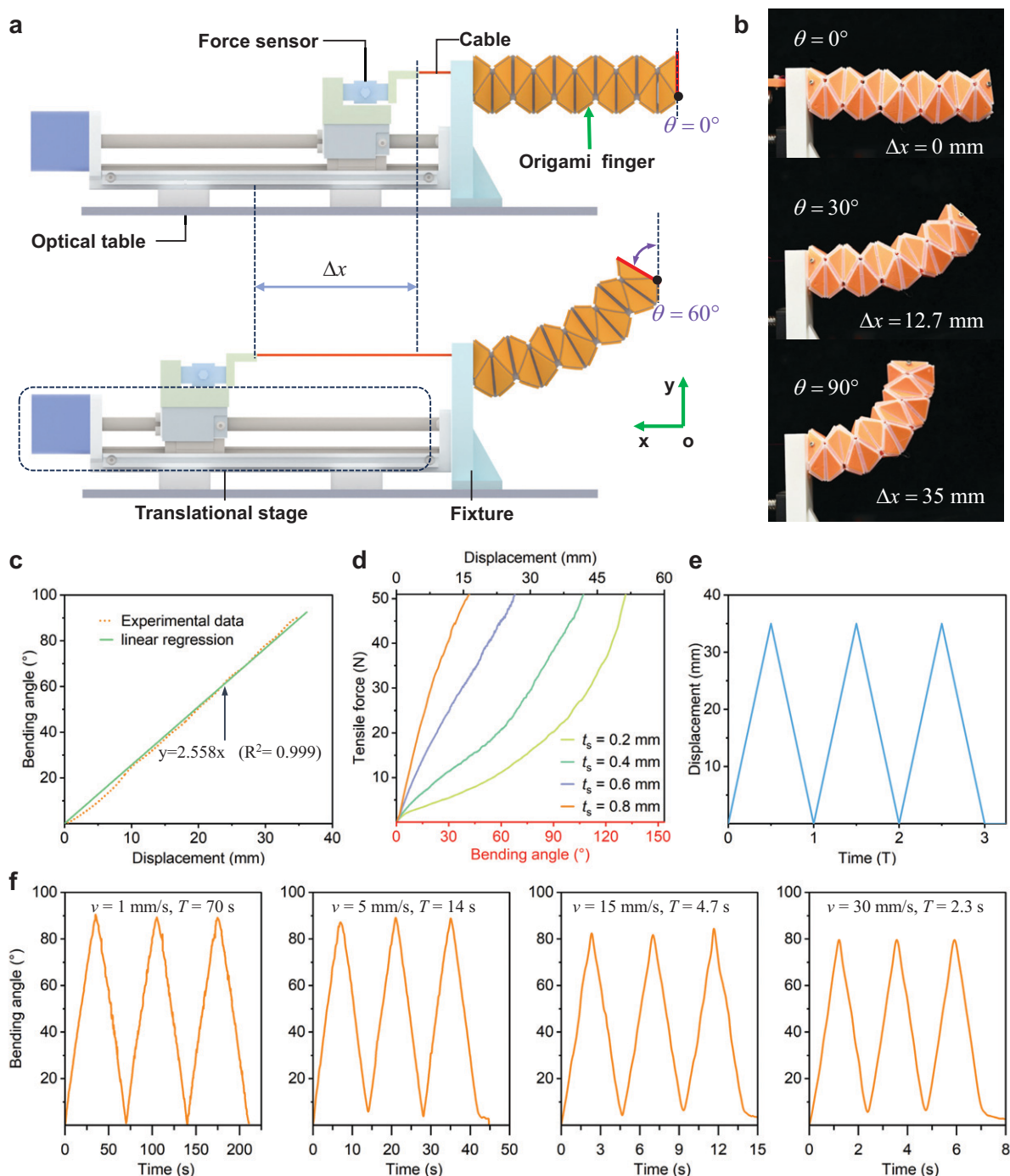


FIG. 7. Experiment on bending an origami finger. **(a)** Schematic diagram of the measurement system. **(b)** Process photos of origami finger bending 90° . **(c)** Displacement versus bending angle of origami fingers during loading. **(d)** Displacement versus cable tension force of origami fingers during loading. **(e)** Time versus displacement of translational stage of the measurement system. **(f)** Time versus bending angle of origami fingers during dynamic response.

angles ($\theta = 0^\circ, 25^\circ, 50^\circ$, and 75°). The data indicate that, for a fixed hinge thickness, the bending stiffness increases with an increase in the bending angle θ . Similarly, at a constant bending angle, an increase in t_s results in higher bending stiffness. As bending stiffness increases, deforming the origami finger becomes more difficult. For instance, with $t_s = 0.2$ mm, the force required at a 5 mm displacement for a 75° bend is 0.321 N, compared to 0.083 N for a 0° bend, showing the maximum force is approximately 3.87 times

the minimum. As t_s increases, the deformation resistance significantly grows. For $t_s = 0.8$ mm, the force needed at a 5 mm displacement for a 75° bend is 2.39 N, much greater than the 0.321 N for $t_s = 0.2$ mm, with the maximum force being about 7.45 times the minimum.

Stiffness directly measures an origami structure's ability to resist elastic deformation under external forces. Since resisting external deformation is inherently a dynamic process, we developed a method for calculating stiffness, as

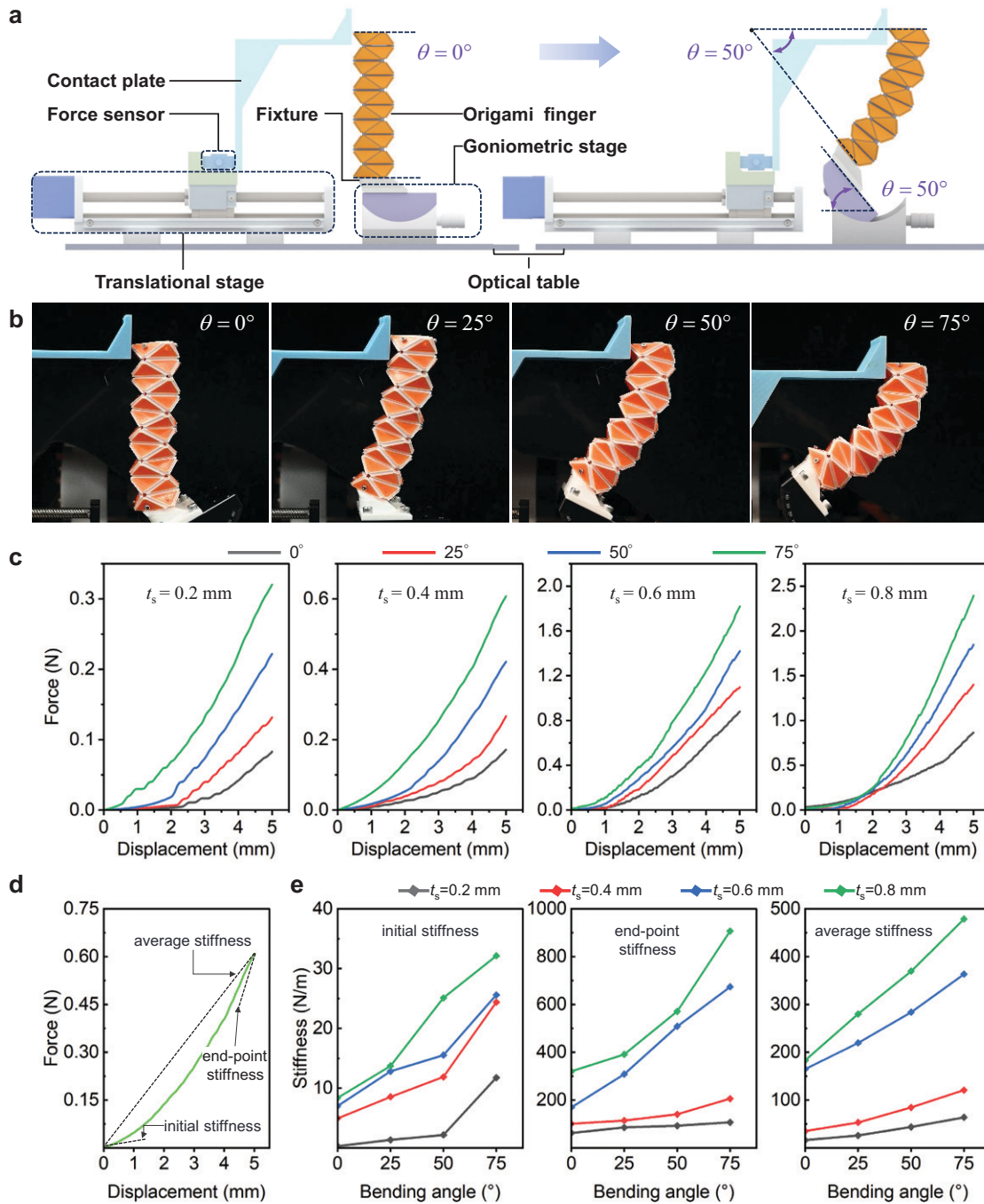


FIG. 8. Stiffness experiment of origami finger. (a) Schematic diagram of the test system. (b) Photographs of initial states at different bending angles. (c) Displacement versus thrust of translational stage during pushing origami fingers. (d) Stiffness calculation method illustration. (e) Stiffness results of the origami finger at different bending angles.

illustrated in Figure 8d. Taking the test curve for $t_s = 0.4$ mm at a bending angle of 75° as an example, the slope at the initial point represents the initial stiffness, whereas the slope at the curve's endpoint represents the endpoint stiffness. The slope of the line connecting the initial and endpoint is considered the average stiffness.

For each curve in Figure 8c, we applied this method to calculate stiffness. The results are displayed in Figure 8e, with initial, endpoint, and average stiffness shown from left

to right. Different t_s values (0.2 mm, 0.4 mm, 0.6 mm, and 0.8 mm) are represented by black, red, blue, and green colors, respectively. Compared to Figure 8c, these results intuitively illustrate that as the origami finger's bending angle increases, it becomes increasingly challenging to deform it under external forces. Focusing on endpoint stiffness alone, the maximum stiffness values at a 75° bend for the different t_s values are 107.1, 206.0, 674.2, and 907.1 N/m, respectively, with the maximum value being 8.47 times the

minimum. From the average stiffness results, the origami finger's stiffness shows a clear linear increase, also peaking at a 75° bend: 64.1, 121.0, 363.6, and 478.8 N/m, where the maximum value is 7.48 times the minimum. Combining these results with the experimental findings from Figure 6, as t_s increases, bending the origami finger becomes substantially more difficult, and its stiffness in resisting external deformation also rises, albeit less steeply. Based on this, we selected $t_s = 0.4$ mm as the optimal design parameter.

Performance of origami-based flexible robotic grippers

The purpose of designing these origami fingers is to assemble an origami gripper capable of functioning as a robotic component, particularly in applications requiring safe human-robot interactions. The gripper is mounted on the end of a commercial robotic arm, serving as a standard tool to grasp daily life objects by leveraging the adaptability of origami robots. Figure 9a shows the origami gripper in a working scenario attached to the end flange of a 6-axis robotic arm. Figure 9b presents the physical prototype, which consists of three origami fingers arranged in a 120° circular configuration. A bus servo motor on the gripper rack drives the gripper by rotating a pulley, which in turn coiled the cables attached to the three origami fingers, causing them to bend or straighten accordingly. This mechanism allows the origami gripper to grasp or release target objects effectively.

The gripper cables are eccentrically routed through one side of the internal space, with one end fixed to an end cap

and the other passing through a mounting hole, allowing relative sliding movement. Figure 9c demonstrates the gripper successfully lifting a 387 g water bottle within 47 s, indicating its ability to handle objects securely and stably, which showcases its safe and effective grasping capability. This work offers both research and practical significance.

Compared to traditional electric grippers used in industrial applications, origami grippers are more suitable for delicate handling tasks, such as those in the food industry, due to their adaptability and safety, which are essential for fragile items. To validate the gripper's ability to handle such objects, we simulated a task of picking and placing fruits into designated boxes, as shown in Figure 10a. Figure 10b–d depicts the gripper grasping and placing various fruits—a spherical orange, an irregularly shaped dragon fruit, and an apple—into packaging boxes. A video demonstrating these processes is shown in Supplementary Video S2. By setting appropriate control parameters for the robotic arm (movement speed less than 20 mm/s), the gripper successfully completed these tasks without damaging the fruits, underscoring its potential utility in the food industry.

Conclusion

In this article, we presented an investigation into the design and optimization of origami robotic grippers fabricated using hard-soft coupled multimaterial 3D printing techniques. Using a kinematic model, we evaluated how variations in unit parameters influence the reachable workspace



FIG. 9. Assembly and grasping performance of the origami gripper. (a) Demonstration of the origami gripper in action. (b) Physical prototype of the origami gripper. (c) Grasping experiment of the origami gripper.

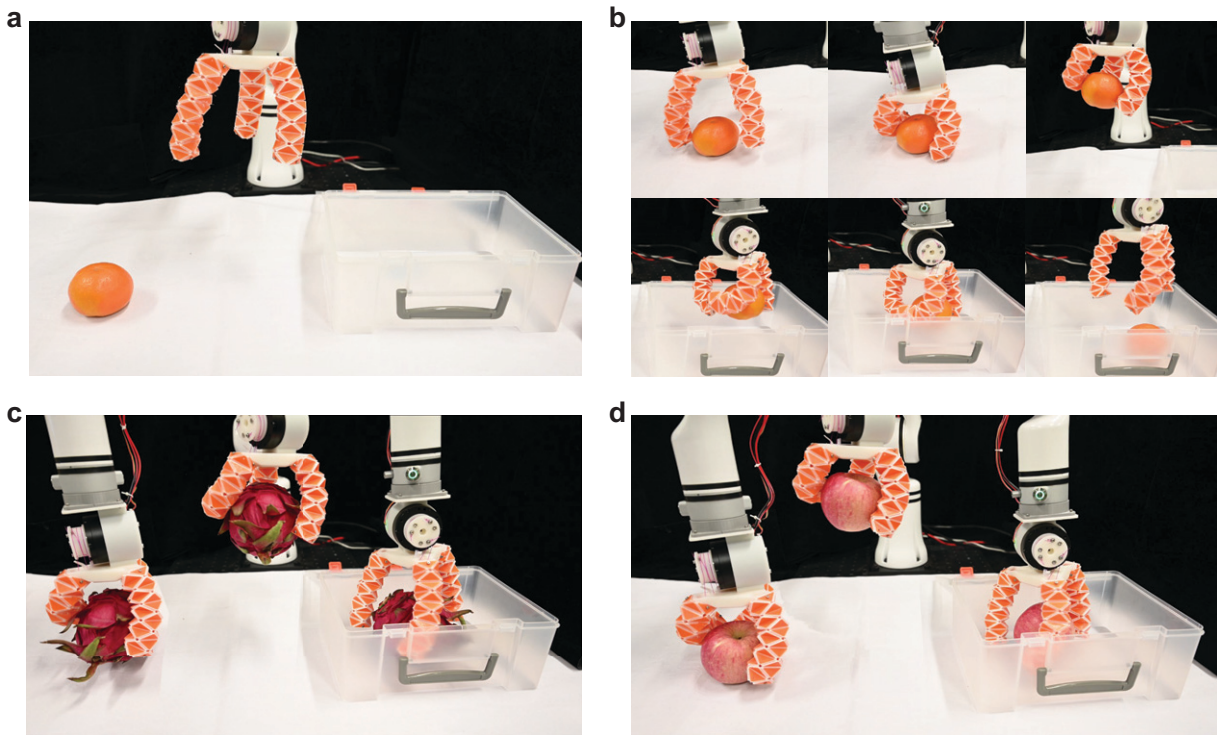


FIG. 10. Flexible grasping experiment. (a) Task setup for the flexible grasping experiment. (b) Grasping and placing an orange. (c) Grasping and placing a dragon fruit. (d) Grasping and placing an apple.

and bending characteristics of the origami finger. We also examined the mechanical response of the Yoshimura origami under different design configurations, where the thickness of hard panels and the width of soft hinges significantly affected stiffness. By experimentally testing origami units with varied thicknesses of soft hinge and width of the valley, we established that increased thickness of soft hinge enhanced the origami's load-bearing capacity, though this concurrently raised bending stiffness. This study further validates that the width of the valley plays a critical role in controlling stiffness and highlights the balance required in design parameters to optimize mechanical performance. For the practical application in robotic grippers, we investigated the relationship between cable displacement, force, and bending angle, illustrating how the dynamic response of the origami structure can be tailored by modifying the thickness of the soft hinge. Our findings show that a smaller thickness of soft hinge allows for greater flexibility, whereas higher values of thickness of soft hinge achieve higher stiffness but limit the maximum bending angle. In conclusion, this research demonstrates the potential of origami-based robotic systems manufactured through hard-soft coupled multimaterial 3D printing, highlighting their versatility, efficiency, and effectiveness.

Author Disclosure Statement

No competing financial interests exist.

Acknowledgments

B.J. acknowledges the financial support by the Shanghai Rising-Star Program (No. 24YF2747700) and the Sponsored by Shanghai Pujiang Program (No. 24PJA129). L.J. acknowledges

the support by the Research Grants Council (Hong Kong) under the Hong Kong PhD Fellowship Scheme.

Funding Information

Q.G. received funding from the National Natural Science Foundation of China (no. 12072142) and the Program of Guangdong Province (no. 2019QN01Z438).

Supplementary Material

Supplementary Data
Supplementary Video S1
Supplementary Video S2

Reference

1. Rus D, Tolley MT. Design, fabrication and control of soft robots. *Nature* 2015;521(7553):467–475.
2. Lin H-T, Leisk GG, Trimmer BA. Soft robots in space: A perspective for soft robotics. *Acta Futura* 2013;6:69–79.
3. Tolley MT, Shepherd RF, Mosadegh B, et al. A resilient, untethered soft robot. *Soft Robotics* 2014;1(3):213–223.
4. Marchese AD, Onal CD, Rus D. Autonomous soft robotic fish capable of escape maneuvers using fluidic elastomer actuators. *Soft Robot* 2014;1(1):75–87.
5. Yu Q, Gravish N. Multimodal locomotion in a soft robot through hierarchical actuation. *Soft Robot* 2024;11(1):21–31.
6. Brown E, Rodenberg N, Amend J, et al. Universal robotic gripper based on the jamming of granular material. *Proc Natl Acad Sci USA* 2010;107(44):18809–18814.
7. Polygerinos P, Wang Z, Galloway KC, et al. Soft robotic glove for combined assistance and at-home rehabilitation. *Robotics and Autonomous Systems* 2015;73:135–143.

8. Zhang J, Li Y, Kan Z, et al. A preprogrammable continuum robot inspired by elephant trunk for dexterous manipulation. *Soft Robot* 2023;10(3):636–646.
9. Khosravani MR, Soltani P, Rolfe B, et al. Static and dynamic characterization of 3D-printed polymer structural elements. *Polymer Testing* 2024;137:108533.
10. Fusco S, Sakar MS, Kennedy S, et al. An integrated micro-robotic platform for on-demand, targeted therapeutic interventions. *Adv Mater* 2014;26(6):952–957.
11. Cianchetti M, Laschi C, Menciassi A, et al. Biomedical applications of soft robotics. *Nat Rev Mater* 2018;3(6):143–153.
12. Blackiston D, Kriegman S, Bongard J, et al. Biological robots: Perspectives on an emerging interdisciplinary field. *Soft Robot* 2023;10(4):674–686.
13. Jin T, Wang T, Xiong Q, et al. Modular soft robot with origami skin for versatile applications. *Soft Robot* 2023;10(4):785–796.
14. Ye Z, Zheng L, Chen W, et al. Recent advances in bioinspired soft robots: Fabrication, actuation, tracking, and applications. *Adv Materials Technologies* 2024;9(21):2301862.
15. Wang X, Guo R, Liu J. Liquid metal based soft robotics: Materials, designs, and applications. *Adv Materials Technologies* 2019;4(2):1800549.
16. Wong DCY, Li M, Kang S, et al. Reconfigurable, transformable soft pneumatic actuator with tunable three-dimensional deformations for dexterous soft robotics applications. *Soft Robot* 2024.
17. Soleimanzadeh H, Rolfe B, Bodaghi M, et al. Sustainable robots 4D printing. *Advanced Sustainable Systems* 2023;7(12):2300289.
18. Mohammadi M, Kouzani AZ, Bodaghi M, et al. Sustainable robotic joints 4D printing with variable stiffness using reinforcement learning. *Robotics and Computer-Integrated Manufacturing* 2024;85:102636.
19. Mohammadi M, Kouzani AZ, Bodaghi M, et al. 3D-printed phase-change artificial muscles with autonomous vibration control. *Advanced Materials Technologies* 2023;8(23):2300199.
20. Zhang Y-F, Zhang N, Hingorani H, et al. Fast-response, stiffness-tunable soft actuator by hybrid multimaterial 3D printing. *Advanced Functional Materials* 2019;29(15):1806698.
21. Jin L, Zhai X, Zhang K, et al. 3D printing soft robots integrated with low-melting-point alloys. *Msam* 2024;3(3):4144.
22. Bächer M, Knoop E, Schumacher C. Design and control of soft robots using differentiable simulation. *Curr Robot Rep* 2021;2(2):211–221.
23. Thuruthel TG, Ansari Y, Falotico E, et al. Control strategies for soft robotic manipulators: A survey. *Soft Robot* 2018;5(2):149–163.
24. Zhang Z, Chen G, Xun Y, et al. Bioinspired rigid-soft hybrid origami actuator with controllable versatile motion and variable stiffness. *IEEE Trans Robot* 2023;39(6):4768–4784.
25. Dezaki ML, Sales R, Zolfagharian A, et al. Soft pneumatic actuators with integrated resistive sensors enabled by multimaterial 3D printing. *Int J Adv Manuf Technol* 2023;128(9–10):4207–4221.
26. Kwok SW, Morin SA, Mosadegh B, et al. Magnetic assembly of soft robots with hard components. *Adv Funct Materials* 2014;24(15):2180–2187.
27. Tang Y, Chi Y, Sun J, et al. Leveraging elastic instabilities for amplified performance: Spine-inspired high-speed and high-force soft robots. *Sci Adv* 2020;6(19):eaaz6912.
28. Chen Y, Wan F, Wu T, et al. Soft-rigid interaction mechanism towards a lobster-inspired hybrid actuator. *J Micro-mech Microeng* 2018;28(1):014007.
29. Lotfiani A, Zhao H, Shao Z, et al. Torsional stiffness improvement of a soft pneumatic finger using embedded skeleton. *Journal of Mechanisms and Robotics* 2020;12(1):011016.
30. Wu Z, Li X, Guo Z. A novel pneumatic soft gripper with a jointed endoskeleton structure. *Chin J Mech Eng* 2019;32(1)–12.
31. Al-Rubaiai M, Pinto T, Qian C, et al. Soft actuators with stiffness and shape modulation using 3D-printed conductive polylactic acid material. *Soft Robot* 2019;6(3):318–332.
32. Zolfagharian A, Gharraie S, Gregory J, et al. A bioinspired compliant 3D-printed soft gripper. *Soft Robot* 2022;9(4):680–689.
33. Zirbel SA, Lang RJ, Thomson MW, et al. Accommodating thickness in origami-based deployable arrays. *Journal of Mechanical Design* 2013;135(11):111005.
34. Morgan J, Magleby SP, Howell LL. An approach to designing origami-adapted aerospace mechanisms. *Journal of Mechanical Design* 2016;138(5):052301.
35. Kim J, Bae J. Self-locking pneumatic actuators formed from origami shape-morphing sheets. *Soft Robot* 2024;11(1):32–42.
36. Melancon D, Gorissen B, García-Mora CJ, et al. Multistable inflatable origami structures at the metre scale. *Nature* 2021;592(7855):545–550.
37. Misseroni D, Pratapa PP, Liu K, et al. Origami engineering. *Nat Rev Methods Primers* 2024;4(1):40.
38. Zhang H, Paik J. Lattice-and-plate model: Mechanics modeling of physical origami robots. *Soft Robot* 2023;10(1):149–158.
39. Miyashita S, Guitron S, Yoshida K, et al. Ingestible, controllable, and degradable origami robot for patching stomach wounds. In: *2016 IEEE International Conference on Robotics and Automation (ICRA)*, IEEE, 2016, pp. 909–916.
40. Ze Q, Wu S, Dai J, et al. Spinning-enabled wireless amphibious origami millirobot. *Nat Commun* 2022;13(1):3118.
41. Bartkowski P, Pawlitzak L, Chevale SG, et al. Programmable shape-shifting soft robotic structure using liquid metal electromagnetic actuators. *Soft Robot* 2024;11(5):802–811.
42. Lee D-Y, Kim S-R, Kim J-S, et al. Origami wheel transformer: A variable-diameter wheel drive robot using an origami structure. *Soft Robot* 2017;4(2):163–180.
43. Rus D, Sung C. Spotlight on origami robots. *Sci Robot* 2018;3(15):eaat0938.
44. Kim S-J, Lee D-Y, Jung G-P, et al. An origami-inspired, self-locking robotic arm that can be folded flat. *Sci Robot* 2018;3(16):eaar2915.
45. Felton S, Tolley M, Demaine E, et al. A method for building self-folding machines. *Science* 2014;345(6197):644–646.
46. Hu Q, Li J, Tao J, et al. Inverse origami design model for soft robotic development. *Soft Robot* 2024;11(1):131–139.

47. Li D, Fan D, Zhu R, et al. Origami-inspired soft twisting actuator. *Soft Robot* 2023;10(2):395–409.
48. Miyashita S, Guitron S, Ludersdorfer M, et al. An untethered miniature origami robot that self-folds, walks, swims, and degrades. In: *2015 IEEE International Conference on Robotics and Automation (ICRA)*, IEEE, 2015, pp. 1490–1496.
49. Lee D-Y, Kim J-K, Sohn C-Y, et al. High-load capacity origami transformable wheel. *Sci Robot* 2021;6(53):eabe0201.
50. Jeong D, Lee K. Design and analysis of an origami-based three-finger manipulator. *Robotica* 2018;36(2):261–274.
51. Suzuki H, Wood RJ. Origami-inspired miniature manipulator for teleoperated microsurgery. *Nat Mach Intell* 2020; 2(8):437–446.
52. Pagano A, Yan T, Chien B, et al. A crawling robot driven by multi-stable origami. *Smart Mater Struct* 2017;26(9):094007.
53. Ze Q, Wu S, Nishikawa J, et al. Soft robotic origami crawler. *Sci Adv* 2022;8(13):eabm7834.
54. Rus D, Tolley MT. Design, fabrication and control of origami robots. *Nat Rev Mater* 2018;3(6):101–112.
55. Zhang C, Zhang Z, Peng Y, et al. Plug & play origami modules with all-purpose deformation modes. *Nat Commun* 2023;14(1):4329.
56. Novelino LS, Ze Q, Wu S, et al. Untethered control of functional origami microrobots with distributed actuation. *Proc Natl Acad Sci U S A* 2020;117(39):24096–24101.
57. Melancon D, Forte AE, Kamp LM, et al. Inflatable origami: Multimodal deformation via multistability. *Adv Funct Materials* 2022;32(35):2201891.
58. Li S, Stampfli JJ, Xu HJ, et al. A vacuum-driven origami “magic-ball” soft gripper. In: *2019 International Conference on Robotics and Automation (ICRA)*, IEEE, 2019, pp. 7401–7408.
59. Ye H, Liu Q, Cheng J, et al. Multimaterial 3D printed self-locking thick-panel origami metamaterials. *Nat Commun* 2023;14(1):1607.
60. Liu Q, Ye H, Cheng J, et al. Stiffness-tunable origami structures via multimaterial three-dimensional printing. *Acta Mech Solida Sin* 2023;36(4):582–593.
61. Xue W, Sun Z, Ye H, et al. Rigid-flexible coupled origami robots via multimaterial 3D printing. *Smart Mater Struct* 2024;33(3):035004.

Address correspondence to:

Qi Ge

Department of Mechanical and Energy Engineering
Southern University of Science and Technology
1088 Xueyuan Ave.
Shenzhen
China

E-mail: geq@sustech.edu.cn

Bingcong Jian
School of Mechanical Engineering
Tongji University
Rm. B401
Kaiwu Building
201804 Shanghai
China

E-mail: bingcongjian@tongji.edu.cn